Power Electronic Systems
Laboratory

Proceedings of the 18th European Conference on Power Electronics and Applications (ECCE Europe 2016), Karlsruhe, Germany, September 5-9, 2016

Active Radial Magnetic Bearing for an Ultra-High Speed Motor

M. Schuck,
D. Steinert,
J. W. Kolar

Eidgenössische Technische Hochschule Zürich
Swiss Federal Institute of Technology Zurich

Active Radial Magnetic Bearing for an Ultra-High Speed Motor

Marcel Schuck[1], Daniel Steinert[2], Johann W. Kolar[1]
[1]Power Electronic Systems Laboratory, Swiss Federal Institute of Technology
[2]Levitronix GmbH
Technoparkstrasse 1, CH-8005 Zurich, Switzerland
Email: schuck@lem.ee.ethz.ch
URL: http://www.pes.ee.ethz.ch

Acknowledgments

The authors would like to thank the Else & Friedrich Hugel Fund for Mechatronics for supporting this work.

Keywords

≪Active damping≫, ≪High-speed drive≫, ≪Induction motor≫, ≪Magnetic bearings≫, ≪Modelling≫.

Abstract

The miniaturization trend of electric machines increases the demand for higher rotational speeds to provide a desired mechanical power level at decreased size. To push the limits of rotor miniaturization, new concepts for an ultra-high speed motor are researched, which employs sub-millimeter size rotors and is capable of achieving rotational speeds above 25 million rotations per minute (Mrpm). The rotor is supported by means of a frictionless active magnetic bearing, which counteracts the gravitational force in vertical direction. Due to the low damping of the rotor, a magnetic bearing is also required in horizontal direction to fully stabilize it. The respective system model, position sensor system and controller design for such a magnetic bearing are outlined in this study. Experimental results demonstrate an increased horizontal damping of the rotor by a factor of more than 100.

Introduction

Increasing the rotational speed of an electric machine allows for decreasing its size for a required power level. This has led to an ongoing miniaturization trend of machines with rising rotational speeds. Drive systems with rotational speeds of up to 1 Mrpm have been demonstrated in the past [1].

The goal of this project is to research new concepts for motors with ultra-high rotational speeds beyond 25 Mrpm in order to extend the limits of conventional machines and overcome the associated challenges in regard to rotor miniaturization, mechanical stress and controllability of highly dynamic systems. As friction losses become significant at such high rotational speeds, contactless magnetic bearings need to be used to reduce bearing friction. Moreover, the rotor is spun inside a vacuum to decrease air friction losses. As the ultimate limit is determined by the centrifugal load of the rotor, small spherical rotors with diameters of less than 1 mm made from ferromagnetic and conductive materials with high tensile strengths are used.

A rotational speed of 23.16 Mrpm has already been reported in 1946 [2] and was achieved with a steel sphere of 0.8 mm in diameter, which was magnetically levitated inside a vacuum tube. However, such high rotational speeds could not be verified in other reported attempts [3]. Therefore, it is a further goal of this work to verify this rotational speed and, ultimately, demonstrate the highest achievable rotational speed with an electric motor.

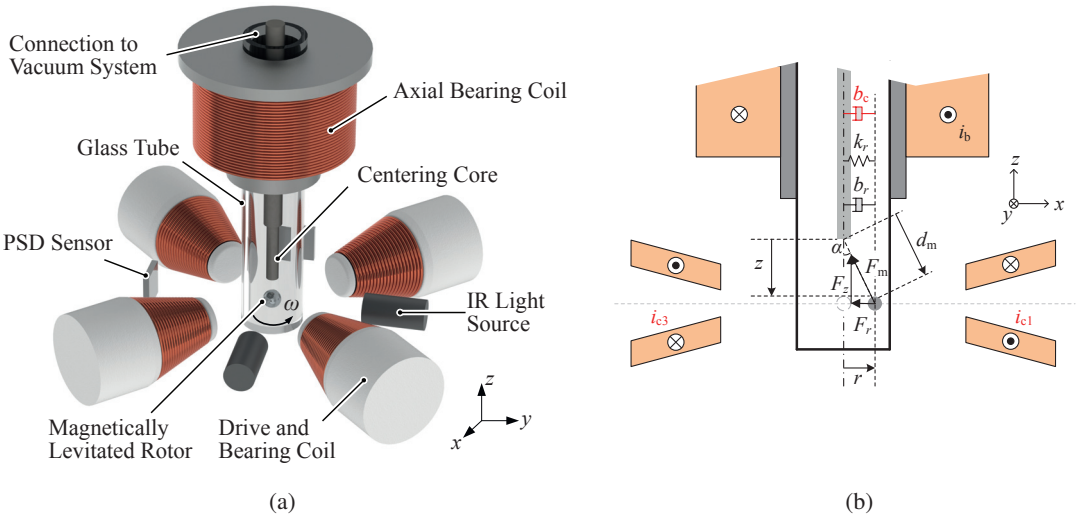

Fig. 1: Three-dimensional (a) and cross-sectional (b) view of the ultra-high speed motor setup.

For magnetic levitation of the rotor an active magnetic bearing (AMB) in vertical (axial) direction is required. As there is almost no air friction acting on the rotor, horizontal (radial) oscillations due to disturbances are almost undamped, causing the magnetic suspension to become radially instable. Radial stability has been achieved by using a passive damping needle that is magnetically coupled to the rotor in the past [4], [5]. This method, however, is highly sensitive to vibrations of the setup [6], requires a complicated adjustment process preceding each experiment, and is increasingly more difficult to apply with decreasing rotor size [7].

To achieve even higher rotational speeds with smaller rotor diameters, an improved radial damping method is required. Therefore, a radial AMB that overcomes the aforementioned shortcomings is presented in this study.

The remainder of this paper is organized as follows: Initially, the overall setup of the spinning ball motor is described and the design of the radial AMB is outlined by analyzing its components in detail. The dynamic model of the system in radial direction is presented followed by the description of the developed optical sensor system, which is necessary for measuring the radial rotor position. The design of the bearing coils, which generate the bearing force in radial direction, is shown and the controller design is described. Finally, experimental results are provided that demonstrate a substantial improvement of the rotor stability through increased radial damping of the system.

Motor Setup

The developed motor setup for achieving ultra-high rotational speeds is shown in Fig. 1(a). The rotor is placed inside a vacuum glass tube and levitated by using an AMB, which consists of a hollow iron core with a copper coil wound around it. A centering core inside the vacuum tube concentrates the magnetic flux and is the center of attraction for the levitated sphere.

The magnetic fields for acceleration of the solid rotor induction machine are generated by four radially-placed drive coils. Eddy currents are induced inside the rotor, which under the influence of the generated magnetic field, are subject to tangential Lorentz forces that accelerate the rotor [8]. The drive coils are also used as actuators for the presented radial AMB.

For the axial and radial magnetic suspension to operate properly, the rotor position has to be measured and controlled continuously. In the developed setup, the position is measured by using a light source that shines onto the rotor. The projected rotor shadow is captured by a two-dimensional position sensitive device (PSD) sensor, which is placed on the opposite side of the glass tube. Two of the aforementioned arrangements are placed orthogonally to each other to measure the rotor position in all spatial dimensions.

Radial System Model

The dynamic behavior of the system in radial direction must be known in order to successfully control its response to disturbances. A cross-sectional view of the motor setup with levitated and radially-displaced rotor is shown in Fig. 1(b). The radial position $r(t)$ of the system can be obtained by employing a damped harmonic oscillator model, which is described by the differential equation

$$\ddot{r}(t) + \frac{b_r}{m}\dot{r}(t) + \frac{k_r}{m}r(t) = \frac{F_\mathrm{c}}{m}, \tag{1}$$

with mass m, radial stiffness k_r, and damping constant b_r. The force in radial direction as applied by the control is denoted by F_c.

Passive radial stiffness

The passive radial stiffness k_r as caused by the centering core is obtained by assuming the system to be linear without saturation effects. The force acting on the ferromagnetic sphere as exerted by the axial bearing coil is derived as

$$F_\mathrm{m}(d_\mathrm{m}, i_\mathrm{b}) = \frac{\partial E_\mathrm{m}(d_\mathrm{m}, i_\mathrm{b})}{\partial d_\mathrm{m}} = -\frac{1}{2}\frac{\Delta L \cdot a}{(1 + a \cdot d_\mathrm{m})^2} \cdot i_\mathrm{b}^2, \tag{2}$$

with E_m, ΔL, a, i_b, and d_m being the energy in the magnetic circuit, the maximum variation of the coil inductance, a setup-dependent constant, the bearing current, and the distance of the rotor to the lower end of the centering core, respectively. The component of this force in z-direction F_z needs to compensate for the gravitational force $F_\mathrm{g} = mg$ that acts on the rotor, from which the required bearing current i_b can be calculated for a given air gap length. Displacing the rotor radially results in a passive centering force directed towards the middle of the core. As i_b is already fixed, it is not possible to actively control the radial force with the same actuator. Calculating the mean airgap length for a flat lower end of the centering core, a rotor with radius r_s, and considering the axial distance z and radial distance r separately as shown in Fig. 1(b) yields

$$d_\mathrm{m} = \sqrt{(z + r_\mathrm{s})^2 + r^2} - \frac{\pi}{4} r_\mathrm{s}, \tag{3}$$

and the force in radial direction is given as

$$F_r(r, z) = F_\mathrm{m}(r, z) \cdot \frac{r}{\sqrt{(z + r_\mathrm{s})^2 + r^2}}. \tag{4}$$

Figure 2 shows a plot of the forces F_z and F_r, normalized with respect to F_z at $\alpha = 0°$, dependent on the displacement angle α. It can be seen that the maximum centering force F_r is significantly lower than the axial force F_z at $\alpha = 0°$. The corresponding radial stiffness k_r around the equilibrium position ($\alpha = 0°$) can be obtained as

$$k_r = \frac{i_{z0}^2 \cdot a \cdot \Delta L}{(1 + a \cdot z_\mathrm{m})^2 (z + r_\mathrm{s})}, \tag{5}$$

where i_{z0} denotes the bearing current that is required to levitate the rotor in its desired vertical equilibrium position z_0.

Radial Damping

The only damping of the rotor in radial direction is caused by the air friction. Therefore, radial oscillations due to disturbances are almost undamped, which causes the magnetic suspension to become instable. The subsequent considerations are carried out for a temperature T of 298.15 K (25° C). Details on the fluid mechanical background of the derivations are outlined in [9].

Under ambient pressure conditions, laminar viscous flow conditions apply for the given dimensions of

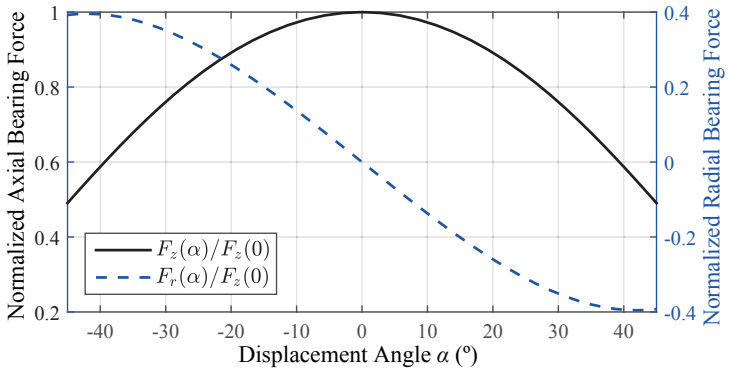

Fig. 2: Normalized active axial force F_z and passive radial force F_r dependent on the radial displacement of the rotor for $z = 2$ mm, $r_\mathrm{s} = 0.5$ mm.

Table I: Model parameters

Parameter	Value	Unit
m	$2.1 \cdot 10^{-6}$	kg
ω_0	53	1/s
b_r	10^{-7}	Ns/m
k_r	5.9	µN/mm

the setup. The corresponding radial damping coefficient due to air friction is obtained based on Stokes' law as

$$b_{r,\mathrm{c}} = 6\pi\eta r_\mathrm{s}, \tag{6}$$

where η denotes the dynamic viscosity of the ambient air. Evaluating (6) for the given setup at ambient pressure yields a damping coefficient in the order of 10^{-7} Ns/m. Final high vacuum pressures in the range of 10^{-6} mbar can be obtained, under which molecular flow conditions apply. To calculate the damping coefficient $b_{r,\mathrm{mol}}$, kinetic gas theory rather than fluid mechanics is applied. A suitable model has been developed in [10], which suggests that the damping coefficient due to the velocity-proportional drag force on a sphere is obtained as

$$b_{r,\mathrm{mol}} = \left(\frac{4}{3} + \frac{\pi}{6}\right) \pi\rho r_\mathrm{s}^2 \bar{c}, \tag{7}$$

where ρ denotes the density and $\bar{c}$ denotes the mean speed of molecules of the surrounding gas. Evaluating (7) at $p = 10^{-6}$ mbar yields a damping coefficient in the order of 10^{-9} Ns/m. Due to the vacuum conditions around the rotor, which are required to achieve ultra-high rotational speeds, the radial damping is decreased by two orders of magnitude, aggravating the problem of instability of the levitated rotor due to weakly damped radial oscillations.

Parameter Identification

To validate the previous theoretical assessments and to gain an accurate model of the practical system, the parameter values of (1) were identified experimentally using a spherical rotor of 0.8 mm in diameter. The resonant frequency ω_n and decay constant σ of radial oscillations of the system as a response to a disturbance were measured. With the assumption of $\omega_\mathrm{n} \approx \omega_0$, which is justified due to the weak damping, the parameters can be calculated as $k_r = \omega_0 m$ and $b_r = 2m\sigma$, respectively. The mass of the sphere, which corresponds to the bob mass of the pendulum, was obtained through calculation based on the density ρ_s of the employed steel as

$$m = \rho_\mathrm{s} \cdot \frac{4}{3}\pi r_\mathrm{s}^3. \tag{8}$$

As passive stability of the rotor under vacuum conditions is difficult to attain, the measurements were carried out under ambient pressure conditions. The results are listed in Table I and are in good agreement with the values as calculated based on the presented analytical model.

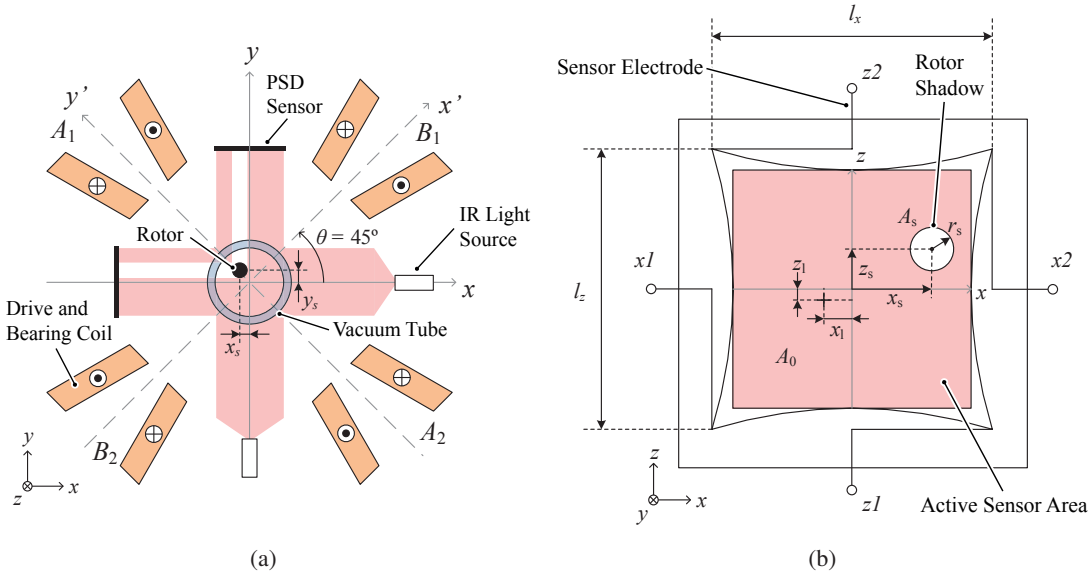

Fig. 3: Cross-sectional view of the motor setup including the two position sensors and the radially-placed combined drive and bearing coils (a). Front view of the employed pin-cushion type PSD sensor (b).

Position Sensor System

In order to actively control the rotor position, a suitable sensor system is required. An optical position measurement system is used in which two PSD sensors (cf. [11]) with an active area of 4×4 mm are located apart by an angle of 90° around the z-axis. An infrared (IR) LED is located at the opposite side of the glass tube pointing towards each sensor as shown in Fig. 3(a). This method allows for fast measurements to be taken and is not impaired by the surrounding magnetic fields as generated by the bearing and drive coils. The sensor outputs currents that are proportional to the centroid of the incident light on its active area. In the given application, the entire active area of the sensor, besides the area where the shadow of the rotor is drawn, is illuminated. The position $(x_\mathrm{l}, y_\mathrm{l})$, which is the centroid of the illuminated area (cf. Fig. 3(b)), can be obtained from the position of the rotor shadow as

$$x_\mathrm{l} = -\frac{A_\mathrm{s}}{A_0 - A_\mathrm{s}} \cdot x_\mathrm{s} \quad \text{and} \quad z_\mathrm{l} = -\frac{A_\mathrm{s}}{A_0 - A_\mathrm{s}} \cdot z_\mathrm{s}, \tag{9}$$

where $A_0 = l_x l_z$ and $A_\mathrm{s} = \pi r_\mathrm{s}^2$ are the active sensor area and the area of the rotor shadow, respectively. The rotor position is then calculated as

$$x_\mathrm{s} = C_x \cdot [(i_{x1} + i_{z2}) - (i_{x2} + i_{z1})] \quad \text{and} \quad z_\mathrm{s} = C_z \cdot [(i_{x1} + i_{z1}) - (i_{x2} + i_{z2})], \tag{10}$$

with i_{x1}, i_{x2}, i_{z1}, i_{z2} being the photo currents as measured at the sensor electrodes $x1$, $x2$, $z1$, and $z2$, respectively. The constants C_x and C_z are given as

$$C_x = \frac{(A_0 - A_\mathrm{s}) \cdot l_x}{2A_\mathrm{s}(i_{x1} + i_{x2} + i_{z1} + i_{z2})} \quad \text{and} \quad C_z = \frac{(A_0 - A_\mathrm{s}) \cdot l_y}{2A_\mathrm{s}(i_{x1} + i_{x2} + i_{z1} + i_{z2})}. \tag{11}$$

The sum of all photo currents remains constant, as the absolute illuminated active area stays the same independent of the position of the rotor (as long as it is fully projected onto the active sensor area).

Signal Acquisition and Processing

To obtain the rotor position information from the measured photocurrents, each current is transformed into a voltage using a transimpedance amplifier. Subsequently, the voltages are amplified and fed into

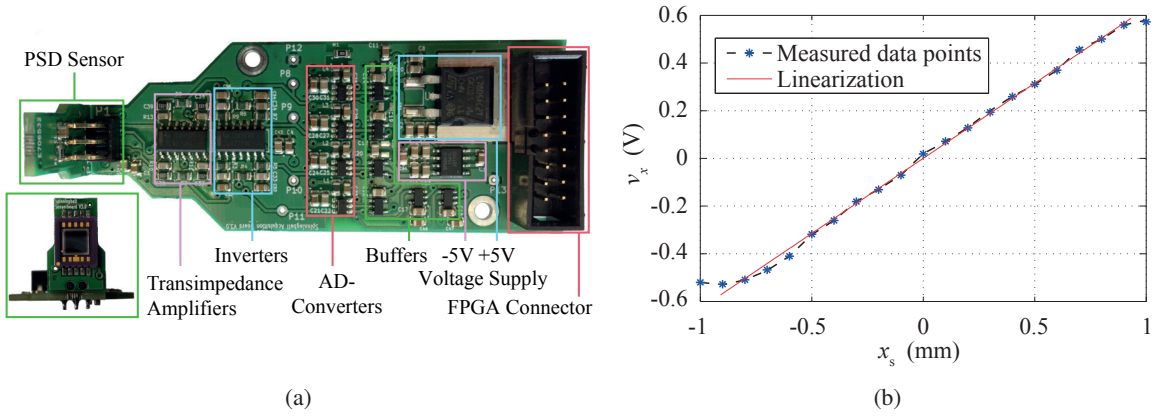

(a) (b)

Fig. 4: Annotated photograph of the designed sensor hardware (a) and measured sensor output for varying radial rotor displacement x_s (b).

AD-converters. The obtained bit stream is processed by an FPGA-based digital control. An annotated photograph of the designed signal acquisition hardware is shown in Fig. 4(a). The measured output of the PSD sensor system for a sphere with 0.8 mm in diameter, which was displaced along the horizontal axis of the sensor at a fixed vertical position, is shown in Fig. 4(b). The voltages at the outputs of the transimpedance amplifiers were measured and v_x was calculated as

$$v_x = (v_{x1} + v_{z2}) - (v_{x2} + v_{z1}). \tag{12}$$

It can be seen that the dependency between the radial position and the output signal is linear for small deviations from the equilibrium position ($x_s = 0$). As the radial position of the sphere approaches the wall of the round vacuum glass tube and the edges of the active sensor area, a non-linear behavior can be observed due to optical effects. The range in which a linear sensor output can be obtained is sufficient for an implementation of the active radial bearing.

Actuators

Due to the limited space around the rotor, the existing drive coils are also used as radial bearing actuators and the corresponding bearing currents are superimposed onto the drive currents. Because of the high drive frequency in excess of 500 kHz ($\widehat{=}$ 30 Mrpm) that is necessary to achieve the desired rotational speeds, and for simplicity, the coils are implemented as air coils. Other implementations using a ferrite stator core are possible and will yield higher motor torques and radial bearing forces but require a thorough consideration of the occurring stator core losses as well as rotor losses. The latter are particularly critical, as the rotor can only be cooled by radiative heat transfer, due to its operation in vacuum. The subsequently outlined considerations are universally applicable and independent of the chosen stator topology.

The achievable motor torque is proportional to the square of the magnetic flux density magnitude at the rotor B_d [8], which is in turn proportional to the current i_d flowing in the drive coils. When applying fundamental frequency switching with the supplying full-bridge inverter, which represents the only feasible option at the desired frequencies, the peak drive current magnitude is given by

$$i_d = \frac{V_{dc}}{2Lf_d}, \tag{13}$$

where V_{dc}, L, f_d, denote the dc-link voltage of the inverter, the inductance of the drive coil, and the fundamental drive frequency, respectively. This shows that the inductance of the coil should be kept as low as possible to achieve a high drive current.

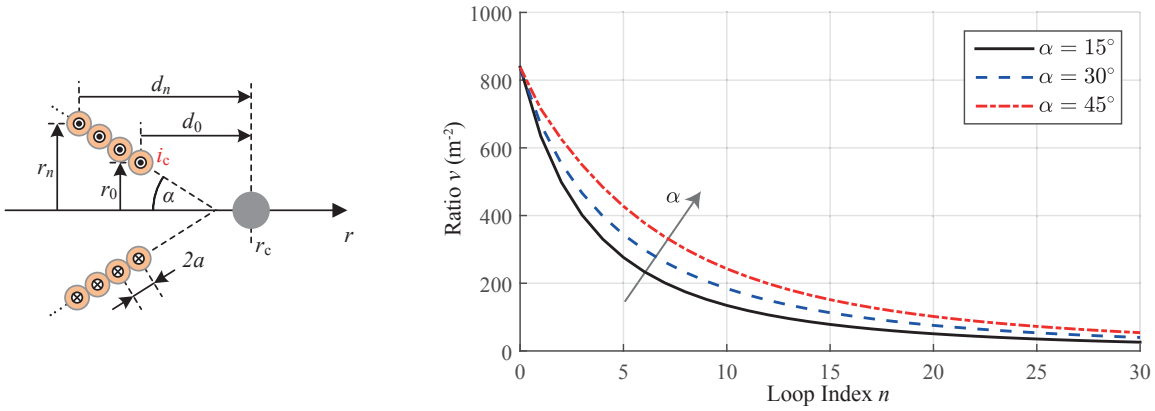

(a) (b)

Fig. 5: Parameters of the conical drive and bearing coils (a) and ratio of the generated flux density at the rotor and the inductance ν for the n^{th} winding (b).

The magnitude of the achievable radial bearing force for a spherical rotor can be approximated as [12]

$$F \approx \frac{4\pi r_s^3}{\mu_0}\left(\frac{\mu_r - 1}{\mu_r + 2}\right) \cdot B_r(r_c) \cdot \frac{\partial B_r(r_c)}{\partial r}, \tag{14}$$

where B_r denotes the magnetic flux density in radial direction as generated by the bearing coils, r_c is the position of the center of the sphere, and μ_r denotes the relative permeability of the rotor material. The achievable bearing force is proportional to the absolute value of B_r at the center of the rotor and its derivative $\partial B_r(r_0)/\partial r$. Therefore, the combined bearing and drive coil must be optimized for generating a high flux density at the rotor while having a low inductance value. A conically-shaped air coil design was chosen as an example, as it facilitates the optimization of its design by means of analytic calculations. For more complicated stator designs, such as the ones employing a ferrite core, FEM simulations are usually required to obtain the achievable bearing force and the resulting coil inductance. The geometry as shown in Fig. 5(a) allows for an increased flux density by locating the individual windings closer to the rotor than with a conventional cylinder coil. However, the increased radii of the windings also increases their inductance value. Exact analytic solutions for the magnetic field as generated by conical helix coils have been presented in the literature [13], yet these results do not allow for an analytic assessment of the problem due to their complexity. Therefore, the coil is approximated by multiple separated concentric loops, for which the magnitude of the flux along the radial axis can be calculated by the Biot-Savart law as

$$B_{r,n} = \frac{\mu_0 \cdot i_b \cdot r_n^2}{2(l_n + r_n^2)^{3/2}}, \tag{15}$$

where i_b, r_n, and l_n denote the bearing current flowing in the loop, the radius of the loop, and the distance of the loop to the center of the rotor for the n^{th} loop, respectively. The inductance of the loop can be approximated by [14]

$$L_n \approx \mu_0 r_n \left[\ln\left(\frac{8r_n}{a}\right) - 2\right], \tag{16}$$

where a denotes the wire radius. If multiple loops are combined to a conical coil, the ratio $\nu = B_{r,n}/(i_b \cdot L_n)$, which relates the flux generated at the rotor to the inductance of the winding, can be calculated for each ring for different semi-angles α of the cone. The value of the derivative of $B_{r,n}$ is almost independent of α. It can be observed that ν decreases for windings which are further away from the rotor and that this decrease is less rapid for higher values of α.

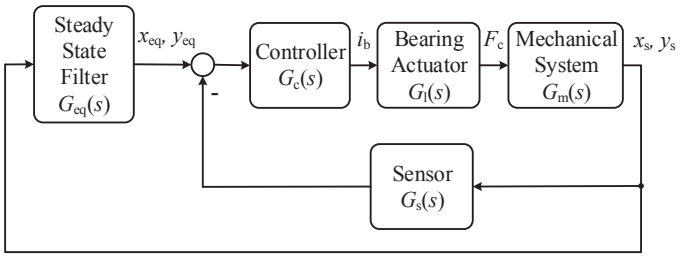

Fig. 6: Block diagram of the control system.

For the practical implementation, a compromise between high flux density at the rotor, low inductance, and low coil current was found by implementing a conical coil with a semi-angle of 15° and three layers of 15 windings each. With this implementation, radial bearing forces in the range of several µN are achievable, which is sufficient for increasing the radial damping of the system.

Controller Design

The radial stability of the rotor is increased by controlling the force generation of the presented radial AMB such that it acts as a second damping element with damping constant b_c (cf. Fig. 1(b)). The block diagram of the control system is shown in Fig. 6 and two controllers are implemented separately for the x and the y direction. As the equilibrium position (x_{eq}, y_{eq}) of the rotor should not be altered by the control, a steady state position filter is used to generate the reference input for the controller. This filter with transfer function $G_{eq}(s)$ is implemented as a moving-average filter over several periods of the radial oscillation signal. A differential controller with assumed ideal transfer function

$$G_c(s) = C_d \cdot s \tag{17}$$

is used to generate the control force F_c that is proportional to the velocity of the oscillating sphere. The transfer function of the bearing coil $G_l(s)$, as obtained based on its series dc resistance R_{dc} and its inductance L_c, is assumed to be 1, due to its electrical time constant being much lower than the mechanical time constant of the system.

The transfer function of the mechanical system is obtained from (1) as

$$G_m(s) = \frac{r(s)}{F_c(s)} = \frac{\frac{1}{m}}{s^2 + \frac{b_r}{m} \cdot s + \frac{k_r}{m}}, \tag{18}$$

and the sensor system is approximated in its linear region by the transfer function

$$G_s(s) = C_s. \tag{19}$$

Combining (17), (18), and (19) yields the open loop transfer function

$$G_o(s) = \frac{r(s)}{F_c(s)} = \frac{1}{m} \cdot \frac{C_s \cdot C_d \cdot s}{s^2 + \frac{b_r}{m} \cdot s + \frac{k_r}{m}}. \tag{20}$$

The corresponding closed loop transfer function is obtained as

$$G_{cl}(s) = \frac{G_o(s)}{1 + G_o(s)} = \frac{k \cdot N_o(s)}{D_o(s) + k \cdot N_o(s)}, \tag{21}$$

where $N_o(s)$ and $D_o(s)$ denote the numerator and the denominator of $G_o(s)$, respectively, and k is the controller gain.

Values of $C_d = 1$ and $C_s = 1$ have been chosen for an initial controller design. From the plot of the root

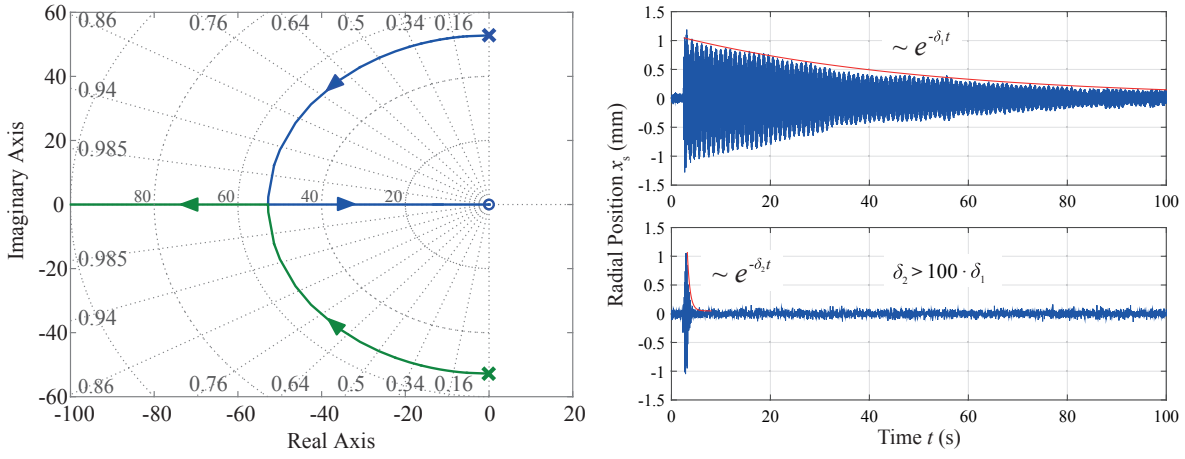

(a) (b)

Fig. 7: Root locus of the control system (a) and measured response of the uncontrolled (top) and controlled (bottom) system to a radial disturbance (b).

locus, which is shown in Fig. 7(a), a suitable value for k is obtained. It can be observed, that the poles of the closed loop system are effectively shifted to the left in the complex plane, which corresponds to an increased damping as k is increased. Choosing relatively small values for k already yields the aperiodic limit of the pendulum.

As the radial bearing coils along the axes x', y' are rotated by an angle of $\theta = 45°$ with respect to the sensor axes x, y (cf. Fig. 3(a)), an angle transformation of the sensor signals has to be carried out. This is performed by using a Givens rotation as

$$\begin{bmatrix} x' \\ y' \end{bmatrix} = \begin{bmatrix} \cos\theta & -\sin\theta \\ \sin\theta & \cos\theta \end{bmatrix} \begin{bmatrix} x \\ y \end{bmatrix} \overset{\theta=45°}{=} \frac{\sqrt{2}}{2} \begin{bmatrix} x-y \\ x+y \end{bmatrix}. \tag{22}$$

Experimental Verification

To verify the performance of the proposed control scheme, it was implemented on an FPGA-based controller and measurements using the prototype of the ultra-high speed spinning ball motor were carried out. Figure 7(b) shows the radial position of the system with a 0.8 mm rotor as a response to an identical disturbance for the uncontrolled (top) and the controlled (bottom) system, respectively. The damping constant of the system was increased by a factor of more than 100, causing radial oscillations to decay in less than 2 s, as opposed to more than 100 s. Similar results can be obtained for even smaller rotors down to 0.5 mm in diameter.

Conclusion

An analytic model for assessing the radial stability of the rotor in an ultra-high speed spinning ball motor has been presented. The design of a contactless optical sensor system, combined drive and bearing actuators and the controller, which are necessary components to implement a radial AMB, have been outlined. The proposed control technique was implemented on an FPGA-based digital controller and its performance was verified through experiments. The results demonstrate a substantially improved rotor stability and an increase in radial damping by a factor of more than 100. The presented radial AMB exceeds the scope of the previously available literature and facilitates the reproducible achievement of rotational speeds beyond 25 Mrpm.

References

[1] C. Zwyssig, J. Kolar, and S. Round, "Megaspeed drive systems: Pushing beyond 1 million r/min," *IEEE/ASME Trans. Mechatronics*, vol. 14, no. 5, pp. 564–574, 2009.

[2] J. W. Beams, J. L. Young, and J. W. Moore, "The production of high centrifugal fields," *Journal of Applied Physics*, vol. 17, no. 11, pp. 886–890, 1946.

[3] A. Boletis and H. Bleuler, "Achieving ultra-high rotating speeds," in *8th International Symposium on Magnetic Bearing, Mito, Japan*, 2002, pp. 539–542.

[4] L. E. MacHattie, "The production of high rotational speed," *Review of Scientific Instruments*, vol. 12, no. 9, pp. 429–435, 1941.

[5] C. Wildmann, T. Nussbaumer, and J. Kolar, "Design considerations for the drive system of an ultra-high speed spinning ball motor," in *Power Electronics Electrical Drives Automation and Motion (SPEEDAM), 2010 International Symposium on*, 2010, pp. 1478–1483.

[6] J. Fremerey, "Apparatus for determination of residual drag torque on small spinning spheres in magnetic suspension," *Review of Scientific Instruments*, vol. 42, no. 6, pp. 753–762, 1971.

[7] J. W. Beams, "Magnetic suspension for small rotors," *Review of Scientific Instruments*, vol. 21, no. 2, pp. 182–184, 1950.

[8] T. Reichert, T. Nussbaumer, and J. W. Kolar, "Complete analytical solution of electromagnetic field problem of high-speed spinning ball," *Journal of Applied Physics*, vol. 112, no. 10, pp. –, 2012.

[9] J. F. O'Hanlon, *A user's guide to vacuum technology*, John Wiley & Sons, 2005.

[10] P. S. Epstein, "On the resistance experienced by spheres in their motion through gases," *Physical Review*, vol. 23, no. 6, p. 710, 1924.

[11] H. Woltring, "Single- and dual-axis lateral photodetectors of rectangular shape," *IEEE Trans. Electron Devices*, vol. 22, no. 8, pp. 581–590, 1975.

[12] M. Schuck, T. Nussbaumer, and J. W. Kolar, "Characterization of electromagnetic rotor material properties and their impact on an ultra-high speed spinning ball motor," *IEEE Trans. Magnetics*, vol. 52, no. 7, 2016.

[13] L. Holmes, "Stability of magnetic levitation," *Journal of Applied Physics*, vol. 49, no. 6, pp. 3102–3109, 1978.

[14] R. S. Elliot, *Electromagnetics: history, theory, and applications*, *IEEE*, 1993.